

Separatrices and basins of stability from time series data: an application to biodynamics

Martin L. Tanaka · Shane D. Ross

Received: 11 February 2008 / Accepted: 20 November 2008 / Published online: 9 December 2008
© Springer Science+Business Media B.V. 2008

Abstract An approach is presented for identifying separatrices in state space generated from noisy time series data sets which are representative of those generated from experiments. We demonstrate how these separatrices can be found using Lagrangian coherent structures (LCSs), ridges in the state space distribution of the maximum finite-time Lyapunov exponent. As opposed to the current approach which requires a vector field in the state space at each instant of time, this method can be performed using only trajectories reconstructed from time series. As such, this paper forms a bridge connecting methods for evaluating time series data with methods used to evaluate LCSs in vector fields. The methods are applied to a problem in musculoskeletal biomechanics, considered as an exemplar

of a class of experimental systems that contain separatrices. In this case, the separatrix reveals a basin of stability for a balancing task, outside of which is a zone of failure. We demonstrate that LCSs calculated from only trajectory data, which samples only portions of the state space, align well with LCSs found using a known vector field. In general, we believe this method provides a fruitful approach for extracting information from noisy experimental data regarding boundaries between qualitatively different kinds of behavior.

Keywords Separatrices · Basin of stability · Time series analysis · Lagrangian coherent structures · LCS · Lyapunov exponents · Recovery envelope

Abbreviations

FTLE Finite-time Lyapunov exponent
LCS(s) Lagrangian coherent structure(s)
 Φ State transition matrix
STM State transition matrix (method)
NN Nearest neighbor (method)

1 Introduction

Increasingly, dynamical systems of interest are defined not by analytical models but by data from experiments or large-scale simulations. Some examples exist in the areas of musculoskeletal biomechanics [1–3] and geophysical fluid dynamics [4–7]. In many cases, researchers want to ascertain if deterministic chaos is

M.L. Tanaka (✉)
Department of Orthopaedic Surgery, Wake Forest
University School of Medicine, Winston-Salem, NC, USA
e-mail: mtanaka@wfubmc.edu

M.L. Tanaka · S.D. Ross
Virginia Tech—Wake Forest University School
of Biomedical Engineering and Sciences,
Blacksburg 24061, VA, USA

S.D. Ross
e-mail: sdross@vt.edu

S.D. Ross
Department of Engineering Science and Mechanics,
Virginia Polytechnic Institute and State University,
Blacksburg 24061, VA, USA

present [2, 8]. This can be achieved by determining characteristic exponents that describe the sensitivity of the solution to initially close starting conditions. One popular technique is to estimate the (maximum) Lyapunov exponent averaged over the sampled portion of state space [9–14]. This method is well suited for analysis of time series data obtained from experiments.

Higher values of the Lyapunov exponent indicate greater divergence rates in state space. When comparing the Lyapunov exponent found for two different experiments, a researcher may conclude that one system is more stable than another. However, this conclusion does not necessarily follow. If the trajectories of both systems remain within the same compact region of state space, then both systems can be considered stable over the finite time evaluated, regardless of the value of the Lyapunov exponent. In order for the system to become unstable, the system trajectory must cross the boundary separating the stable and unstable (or we might say, failure) regions of state space.

The locations of these boundaries can be found by extracting additional information contained within the time series data. Rather than averaging the Lyapunov exponents over state space to obtain a single scalar value as traditionally done, one can generate a maximum Lyapunov exponent *field*. This field quantifies the trajectory divergence rate at different locations in state space. This state space perspective can lead to a better understanding of the system's behavior through identification of boundaries between qualitatively different behaviors. To find these boundaries, we borrow techniques developed for the analysis of fluid flows, namely Lagrangian coherent structures (LCSs) developed initially by Haller et al. [15–19]. From the fluid flow perspective, the term “Lagrangian” is associated with following particle trajectories in state space, and “coherent structures” are patterns that emerge by studying these trajectories. Despite its origin in fluid mechanics, the analogy of looking at structures that emerge in state space carries over to other dynamical systems. Following Shadden et al., we consider LCSs as ridges of the finite-time Lyapunov exponent (FTLE) field [6]. These ridges indicate the location of a separatrix demarking the boundary between qualitatively different kinds of motion. In general, LCSs are found by generating a FTLE field *from the vector field* of the system. However, vector fields are usually unavailable in biomechanics experiments where often only a small number of state variables are measured over time.

In this paper, we apply the LCS method to a rigid body biodynamics problem to identify state space boundaries that are assumed to be time independent. We show that the LCSs can be generated from individual trajectories obtained from time series data without the need of a full vector field at each instant in time. LCSs have previously been shown to be robust with respect to noise [17, 19], making them attractive for use in experimental data analysis where noise sensitivity is an important issue [20–22].

In this paper, we are primarily interested in identifying boundary structure in the state space—from simulated or experimental data—using the LCS approach, boundaries which though important for determining possible behaviors in an experimental system, have gone largely ignored. We are not at this point concerned with precise measurements of the LCS, which we leave as further work. We believe it suffices merely to demonstrate that LCSs, even coarse-grained LCSs, can be obtained from simulated or experimental data.

The organization of the paper is as follows. The introduction is divided into subsections. Section 1.1 describes some potential applications of LCS to biomechanics. Section 1.2 provides background on techniques used to calculate the FTLE field. Section 1.3 describes how, beginning with vector field data, LCSs can be found in the FTLE field using traditional fluid mechanics methods. As biomechanics experiments commonly generate time series data, not vector field data, existing methods to find LCSs are not immediately applicable. Section 1.4 illustrates the approach commonly applied to time series data to find the maximum Lyapunov exponent.

Currently there are no published methods for determining LCS from time series data. Therefore, Sect. 2 presents two new methods for this purpose, the Nearest Neighbor (NN) method (Sect. 2.1) and the State Transition Matrix (STM) method (Sect. 2.2). These methods form a bridge between the traditional methods (Sects. 1.3 and 1.4) and allow LCSs to be found from time series data. Section 3 describes the wobble chair, an unstable seat apparatus that is used to experimentally evaluate torso stability in human subjects. A mathematical model of the wobble chair is described in Sect. 4.

Section 5 is divided into subsections which describe the nonlinear simulations and compare the LCS detection methods. In Sect. 5.1, traditional methods for finding the LCS (Sect. 1.3) are applied to a deterministic and conservative version of the wobble chair

model. The vector field needed for this analysis is generated from the equations of motion. Random noise perturbations are added in Sect. 5.2 and the analysis is repeated using the same method. Section 5.3 describes the generation of simulated experimental data in the form of a time series. This time series data is generated using a forward dynamic simulation of the wobble chair model. Since the simulated experimental data is generated using the same equations of motion, the time series will have the same underlying dynamics as the vector field. This will allow for easy comparison of all results within Sect. 5. In Sect. 5.4, the Nearest Neighbor (NN) method is applied to the time series data and analyzed over different evolution times. Section 5.5 demonstrates the application of the State Transition Matrix (STM) method to the simulated experimental data. A comparison is made between the two new methods and the sensitivity of each method to evolution time is evaluated. The sensitivity of the STM method to the size of the point cloud of initial conditions is described in Sect. 5.6. Section 5.7 describes the sensitivity of the measured LCS locations to the quantity of data by evaluating the sharpness of the LCS ridge; we compare LCSs generated from data sets with as little as two trials up to as many as 100. Conclusions and acknowledgments are given in the last two sections.

1.1 Applications of LCSs to biomechanics

LCSs have previously been used to analyze dynamical systems defined by fluid flow fields [19, 23], analytical biochemical models [24], and low degree of freedom mechanical systems [25]. To our knowledge, the work presented herein is the first application of LCSs to time series data with the absence of a vector field. Biomechanical experiments commonly provide data in this form, where no underlying vector field is known. The biodynamics problem analyzed in this paper may be categorized into a class of biomechanics problems that contain separatrices. There exists a variety of potential applications for these methods in which two or more qualitatively different types of behavior or movement exist. A few examples are illustrated below.

In biomechanics, a separatrix or recovery envelope exists between standing and falling. Standing with postural sway is a distinctly different type of motion from falling. During standing, the body remains in the

vicinity of an equilibrium position and may be characterized as dynamically stable over a suitable finite-time horizon. Compare this motion to falling where the body rapidly diverges from the vicinity of the equilibrium position at an increasing velocity. In falling, the body behaves unstably with respect to the neighborhood of the upright vertical position. If one allows an experimental subject to take a step during fall recovery, another boundary will develop. Now three qualitatively different motions exist: standing, recovering from a fall with one step, and falling. Each type of motion is divided from the other by a separatrix. Extending this theory, a state space diagram with multiple fronts may be generated.

Previous studies have investigated the range of forward and backwards lean that can be attained while maintaining an upright posture without stepping [26–28]. These studies considered the system to be quasi-static, where stability is controlled by muscle strength, base of support and the location of the center of mass. By analyzing the results of these studies, a stable region may be defined in one state space dimension (position) based on the above parameters. Pai et al. expanded this work to two dimensions by including velocity in the mathematical models [29, 30]. Pai used vector fields defined by the system's differential equations to determine regions of stability for balance recovery. Although this work expanded the evaluation of stability into state space, only a small portion of state space was evaluated, and errors in the governing equations resulted in criticism [31].

A problem comparable to standing postural sway is the challenge of maintaining torso stability. In this case, a separatrix exists delineating stable torso sway from unstable and potentially injurious motion (analogous to “falling”). In our laboratory, we study torso stability using an experimental apparatus known as the wobble chair. In addition to its obvious importance to maintaining balance and avoiding falls, torso stability is necessary to avoid excessive deformations in the lumbar spine, which has been associated with low back injury and pain [32, 33].

The computation of finite-time Lyapunov exponents from experimental data has been used to quantify local dynamic stability during locomotion [1, 3]. However, separatrices between dynamically stable walking/running could also be evaluated using the methods developed in this paper.

1.2 Calculation of the FTLE

In this section, we briefly review some mathematical preliminaries regarding stability or sensitivity of trajectories. Suppose we are given a reference trajectory $x(t)$ going from x_0 at time t_0 to x_1 at time t_1 . We assume the trajectory evolves under the dynamical equations of a time-independent (autonomous) system

$$\dot{x} = f(x), \quad x \in \mathbb{R}^n. \tag{1}$$

This equation describes a flow field or vector field. The sensitivity of the reference trajectory is discussed below.

Let trajectories of the system (1) with $x(t_0) = x_0$ be denoted by $\phi(t, t_0)$. In other words, $\phi(t, t_0) : x(t_0) \mapsto x(t)$ denotes the flow map of the dynamical system (1), mapping ‘‘particles’’ (or the system’s state) from their initial location at time t_0 to their location at time t . For our purposes, we will denote the flow map as $\phi(t, t_0; x_0)$, or simply $\phi(t; x_0)$, so that the dependence on the initial condition $x(t_0) = x_0$ is made clear.

Consider a second trajectory that starts slightly away from the reference trajectory $x(t)$, i.e., starts from the perturbed initial vector $x_0 + \delta x_0$ at time t_0 . As the trajectories evolve, the vector displacement (or perturbation vector)

$$\delta x(t) = \phi(t; x_0 + \delta x_0) - \phi(t; x_0) \tag{2}$$

will also evolve. For our purposes, the ‘‘second trajectory’’ might be the result of another experimental trial or another portion of the same trajectory, separated by a sufficient amount of time to avoid a substantial auto-correlation. We discuss this further below.

The linear relationship between small initial perturbations and perturbations at some time t is

$$\delta x(t) = \Phi(t, t_0)\delta x_0, \tag{3}$$

where $\Phi(t, t_0) = \frac{\partial \phi(t; x_0)}{\partial x_0}$ is the state transition matrix (also known as the fundamental matrix). The state transition matrix can be viewed as a deformation gradient. If an (infinitesimal) n -dimensional spherical cloud of particles is placed about the reference trajectory, then after an evolution time $T = t - t_0$, the cloud will have expanded in some directions and compressed in others to form an n -dimensional ellipsoid (Fig. 1).

The matrix $\Phi(t, t_0)$ contains information about this expansion and contraction as well as the rotation of the initial cloud of particles due to the locally deforming nature of the flow.

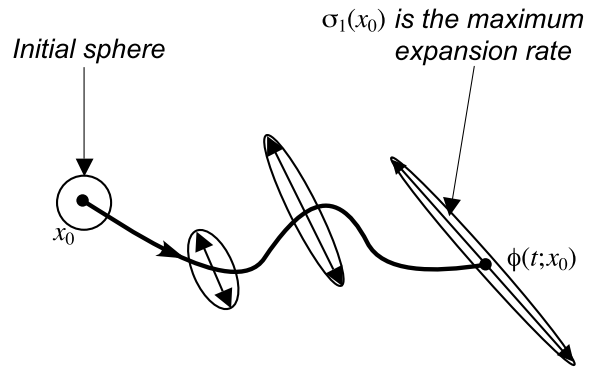


Fig. 1 The state transition matrix is a deformation gradient about the reference trajectory describing how an initially spherical small cloud of initial conditions deforms into an ellipsoid

Suppose there exists a state transition matrix over some interval, $\Phi(t, t_0)$. The size of the final perturbation at time t is given by

$$\|\delta x(t)\|^2 = \delta x_0^* [\Phi(t, t_0)^* \Phi(t, t_0)] \delta x_0, \tag{4}$$

where $\|\cdot\|$ is the vector norm on \mathbb{R}^n , A^* denotes the transpose of the matrix A , and the perturbations δx_0 are considered as column vectors. The symmetric matrix

$$C = \Phi(t, t_0)^* \Phi(t, t_0), \tag{5}$$

is the finite-time right Cauchy–Green deformation tensor [6]. The matrix C is a rotation-independent measure of deformation; it gives the square of the local change in distances due to deformation [34, 35]. Since C is a symmetric, positive definite matrix, it has n real, positive eigenvalues [36, 37].

One can associate with point x_0 a maximum finite-time Lyapunov exponent (FTLE), given by

$$\sigma_1(x_0) = \frac{1}{|T|} \ln \sqrt{\lambda_{\max}(C)}, \tag{6}$$

where $T = t - t_0$ is the finite duration over which expansion is measured and $\lambda_{\max}(C)$ is the maximum eigenvalue of C with the corresponding (normalized) eigenvector $\hat{e}_1(t_0)$. In other words, if δx_0 is along $\hat{e}_1(t_0)$ at time t_0 , then maximum stretching occurs over the time T and the length of the perturbation vector becomes

$$\|\delta x(t)\| = e^{\sigma_1(x_0)T} \|\delta x_0\|, \tag{7}$$

where $t = t_0 + T$ [6].



Fig. 2 Flow chart depicting how LCSs are traditionally determined

1.3 Traditional method of computing LCSs

Lagrangian coherent structures (LCSs) are separatrices in state space, separating qualitatively different kinds of motion. These separatrices are co-dimension one boundaries in state space, i.e., $(n - 1)$ -dimensional surfaces partitioning n -dimensional space. Methods to find LCSs from vector fields are well established [6, 19, 37].

Briefly, the existing method to calculate LCSs includes the measurement or calculation of a generally time-dependent vector field at each instant in time (Fig. 2). Typically, a regular grid of initial state space locations is allowed to evolve due to the vector field, yielding a set of trajectories. From these trajectories the state transition matrix (Φ) is computed, which describes the expansion/contraction and rotation of clouds of initial conditions at the grid points. Recall that Φ is dependent upon the initial location in state space, the initial time, and the evolution time. The FTLE field is computed from Φ and describes the rate of local divergence. LCSs are identified as the ridges in the FTLE field, and they generally correspond to boundaries and state space transport barriers between qualitatively different kinds of behavior. Since the locations of these boundaries are generally changing in a time-dependent flow field, the vector field must be available at each instant of time.

In order to illustrate why ridges develop in the FTLE field at LCSs, consider the phase plot of a pendulum (Fig. 3). In this schematic representation, the circular cloud of initial conditions labeled 1 lies totally within the low energy region of state space, circular cloud 3 lies totally within the high energy region, and circular cloud 2 lies partially within the low and high energy regions. A LCS exists at the boundary between these two regions. It locates a separatrix between low energy oscillating and high energy orbiting movement of the pendulum, two distinctly different types of system behavior. Over time, circular cloud 1 evolves into an ellipse, but since the trajectories of

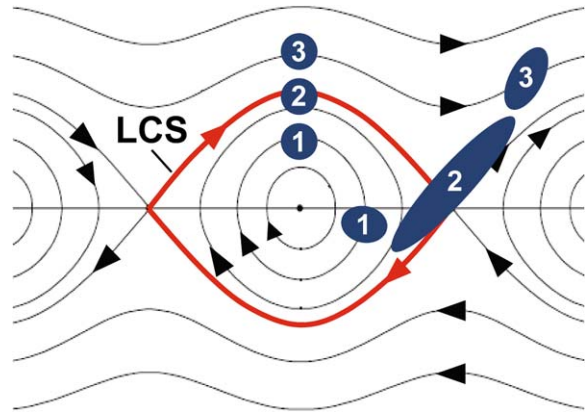


Fig. 3 Effects of a separatrix on the divergence of a cloud of initial conditions. The divergence is high for a cloud of initial conditions with portions of the cloud on opposite sides of a separatrix, cloud 2. This separatrix (a heteroclinic cycle) in the underlying system can be detected as a ridge in the FTLE field, i.e., an LCS

all the points within the cloud are generally similar, only a slight amount of stretching occurs. This slight stretching result is measured as a small FTLE associated with the cloud 1's initial location in state space. Similarly, circular cloud 3 also results in a small value for the FTLE. Portions of circular cloud 2 lie on both sides of the LCS. As the trajectories evolve, the upper portion of the cloud generally flows with cloud 3 while the lower portion tends to flow with cloud 1. These divergent flows cause dramatic stretching of the ellipse and result in a large FTLE associated with the initial location of cloud 2. If this process is repeated over the entire state space, high FTLE values will occur all along the LCS. A FTLE field can be illustrated as the plot of these FTLE values at their associated state space locations, revealing a “volcano shaped” structure at the LCS.

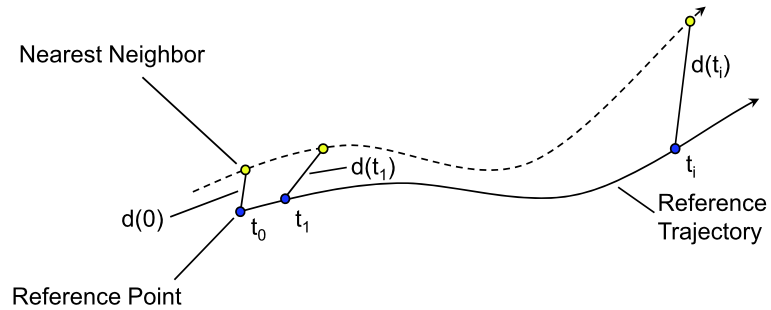
1.4 Traditional approach to time series data

Data collected during biomechanical experiments is often in the form of a low-dimensional time series.



Fig. 4 Flow chart depicting how FTLE are traditionally determined from time series data

Fig. 5 The maximum FTLE is found by calculating the rate of divergence of neighboring trajectories



A common approach in time series analysis is to calculate the maximum FTLE for the entire time series [1, 3, 11, 13, 38–41]. One can assume that the direction of maximum expansion dominates the dynamics of perturbations in arbitrary directions [13]. Under this assumption, we take (7) to hold for all perturbation vectors regardless of their initial state space direction. This will result in a lower bound approximation to the actual value since the perturbation direction will not be exactly aligned with the direction of maximum expansion. As our concern is now focused on the maximum FTLE, hereafter we will refer to the maximum FTLE as simply the FTLE. Traditionally, the FTLE for the time series is estimated by evaluating the rate of separation of neighboring trajectories (Fig. 4).

In order to understand how the FTLE is determined from time series data, consider the reference trajectory shown in Fig. 5. Initially, the first point in the time series is established as the reference point. The nearest neighbor to the reference point in state space is then identified. When finding the nearest neighbor, points are excluded that lie close to the reference point in time in order to avoid a strong correlation with the reference point. The reference point and its nearest neighbor are evolved forward in time-generating trajectories. The FTLE is calculated based on the rate of divergence of these trajectories. Each point in the data set is sequentially evaluated by considering it to be a reference point. Traditionally, the FTLE is averaged over time and space to yield a single scalar value [2, 3, 11, 13]. However, instead of an average value of the

FTLE field, we consider features of the FTLE field itself.

2 New methods for computing LCS from time series data

Our methods create a bridge between the traditional methods described above, allowing LCS to be found from time series data. Two variations exist depending on the location where the bridge is formed (Fig. 6). The Nearest Neighbor (NN) method retains most of the method traditionally used to evaluate time series data. However, rather than averaging the FTLE over the time series to obtain a single scalar value, the FTLE is associated with a state space location to generate a FTLE field. In the State Transition Matrix (STM) method the transition occurs earlier. Instead of identifying a pair of nearest neighbors for evaluation, a virtual cloud is created by selecting neighbors in each dimension of state space. Virtual clouds are evolved in order to estimate the state transition matrix from which an estimate of the FTLE field can be obtained, which is theoretically more accurate than that obtained from the NN method.

2.1 Nearest neighbor method

Unlike vector field data which are much richer, a single trajectory only contains information about one point in state space at any instant of time. In order

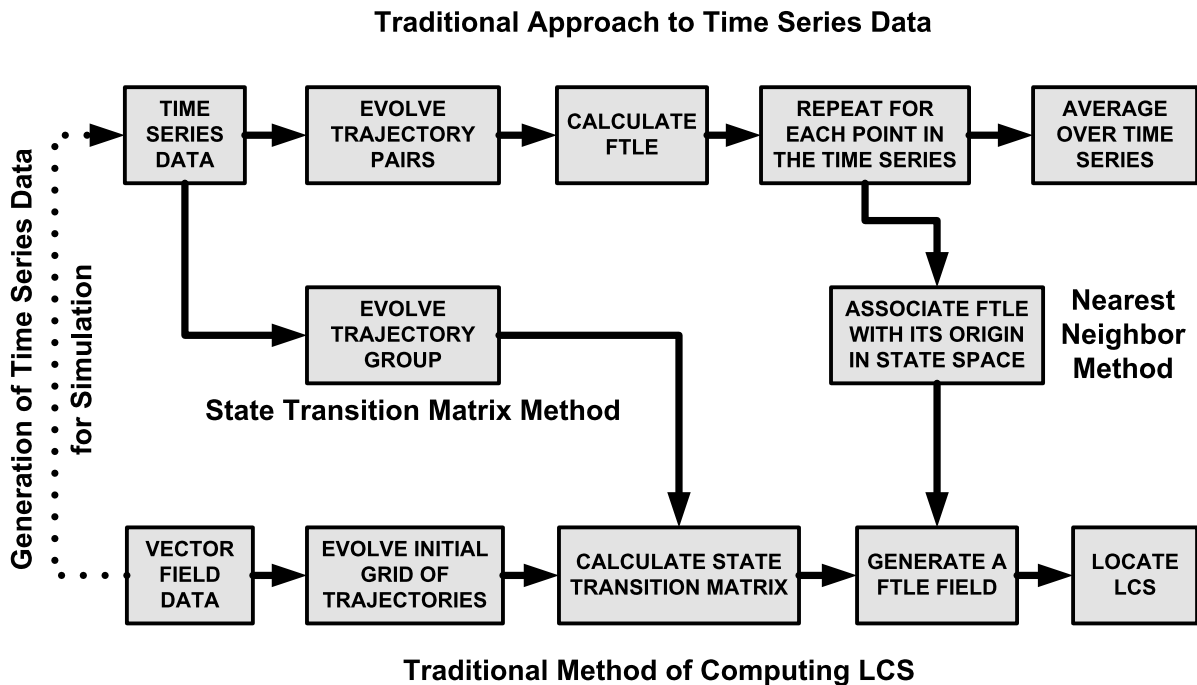


Fig. 6 The new methods create a bridge between the traditional method of analyzing time series data and the methods traditionally used to compute LCS

to compensate for this deficiency in information, data are collected as the trajectory explores different locations in state space over the duration of the experiment. Since the system is assumed to be autonomous, these data can be combined to generate a FTLE field even though the locations in state space may have been explored at times separated by several seconds or minutes. Furthermore, the lack of a vector field introduces new challenges. Unlike a vector field which is continuous over space, time series data, viewed as trajectories, may be sparse or absent in many regions of state space. As a result, the FTLE field may be incomplete, and only portions of the state space may be evaluated. Therefore, an important aspect of both an experiment and a simulation is that the collection of trajectories sample as much of the state space as possible, particularly those portions that contain important boundaries. This is especially pertinent when trying to locate LCSs because it is not possible to experimentally determine their locations, unless data is available on both sides of the structure.

The NN method is identical to the traditional method for calculating FTLE from time series data until the last step (see Fig. 6). In this new method, in

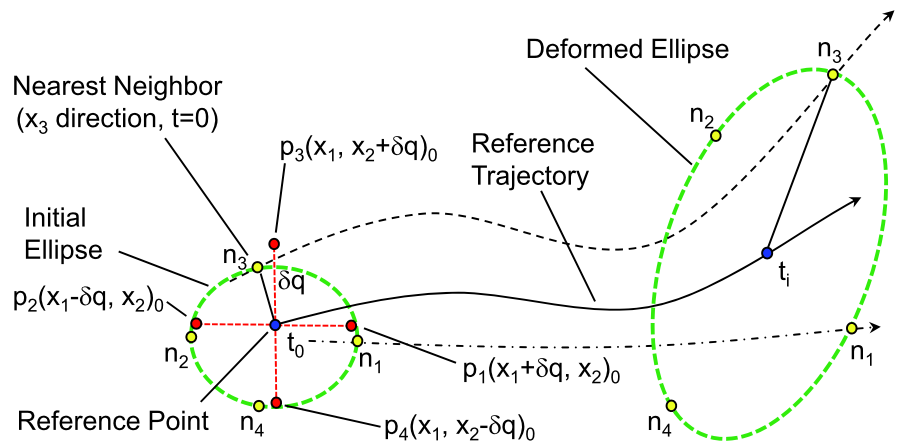
addition to storing the value of the FTLE, the state space location of the reference point is also stored for each point in the time series. In doing so, each FTLE value calculated is associated with a specific location in state space. This matrix of data is used to generate a surface using MATLAB (MathWorks, Natick, MA), particularly the functions (`linspace`, `meshgrid`, `griddata`). A Gaussian filter (`fspecial('gaussian', 7, 3)`) is used to smooth the surface using MATLAB (`imfilter`). This surface is an approximation to the FTLE field. Within the FTLE field, LCS are found by inspection or by rigid extraction methods [6].

We note that the state-space-averaged FTLE can be obtained by computing the average of the FTLE field over the sampled region of state space. This provides a link between the new NN method and the traditional method for finding an averaged Lyapunov exponent from time series data.

2.2 State transition matrix method

Similar to the traditional method used to find the FTLE from time series data, neighboring trajectories are also

Fig. 7 The maximum FTLE is found by calculating the growth of perturbation vectors in multiple state space directions over the time $T = t_i - t_0$. We make the assumption that the maximum FTLE dominates the evolution of the perturbation vectors



evaluated in the STM method. As before, a reference point and its corresponding trajectory are selected (Fig. 7). From the reference point, a target location (p_1) is identified that is a perturbation distance δq from the reference point. This first target is located in the positive direction of the first state-space dimension. The data point closest to p_1 on another trajectory is then found, n_1 . The other trajectory can be from either a different run of the experimental trial or another portion of the same trial separated by a sufficient amount of time to avoid autocorrelation. This process is repeated for each direction (positive and negative) in each dimension of state space, yielding $2n$ neighbors for each reference point. The state transition matrix, Φ , is calculated by evolving the trajectories of these $2n$ neighbors. As a simple example, consider the $n = 2$ dimensional case where the state is $\mathbf{x} = (\theta, \dot{\theta}) = (x, y)$. In this case,

$$\Phi(\mathbf{x}, T) = \begin{bmatrix} \frac{x_{n_1}(t_0+T) - x_{n_2}(t_0+T)}{x_{n_1}(t_0) - x_{n_2}(t_0)} & \frac{x_{n_3}(t_0+T) - x_{n_4}(t_0+T)}{y_{n_3}(t_0) - y_{n_4}(t_0)} \\ \frac{y_{n_1}(t_0+T) - y_{n_2}(t_0+T)}{x_{n_1}(t_0) - x_{n_2}(t_0)} & \frac{y_{n_3}(t_0+T) - y_{n_4}(t_0+T)}{y_{n_3}(t_0) - y_{n_4}(t_0)} \end{bmatrix}, \quad (8)$$

where the subscripts n_1, n_2, n_3 , and n_4 indicate the neighbor in the positive θ direction, negative θ direction, positive $\dot{\theta}$ direction, and negative $\dot{\theta}$ direction, respectively. Once the state transition matrix at point \mathbf{x} is estimated, the FTLE at the point can be computed via (5) and (6). Like the traditional time series method, each point in the data set is sequentially evaluated by considering it to be a reference point. LCSs can be found using the traditional method for computing LCSs described above.

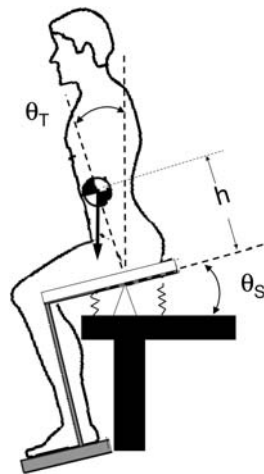
Unlike previous methods, the approach described in this paper constructs a FTLE field using only trajectory data. This eliminates the need for a vector field, which may not be accessible in an experimental setting. Of course, an FTLE field obtained in this way will be limited to the portion of state space sampled by trajectories.

3 Experimental test apparatus

The wobble chair has been used to isolate movement of the lumbar spine in order to gain a better understanding of the dynamics utilized to maintain torso stability and prevent injury (Fig. 8) [38–41]. The wobble chair consists of a seat pan and seat supported by a central ball joint. Stabilizing springs are located at the front, back, left and right of the ball joint and help to support the seat. These springs may be moved closer or further from the central pivot point to modify the amount of restorative torque provided by the springs at any given seat angle. Wobble chair experiments are typically performed at spring distances where the destabilizing gravitational moment exceeds the stabilizing spring torque. This configuration is statically unstable and neuromuscular control must be provided for the participant to maintain his/her balance on the seat. The wobble chair is able to tilt in the sagittal (forwards and backwards) and frontal (left and right) body planes, but rotation in the transverse plane and translation in all planes are restricted.

The wobble chair and experimental protocol are designed to minimize relative movement within the

Fig. 8 The wobble chair is an apparatus designed to isolate the movement of the low back to determine torso stability (adapted from [38, 42])

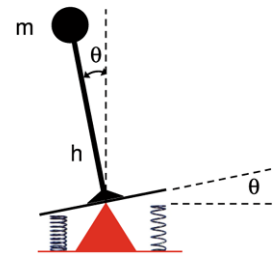


lower body and within the upper body, in order to isolate the effect of relative motion between the lower and upper body. A leg rest is rigidly attached to the seat with the purpose of minimizing relative movement of the legs. Furthermore, the pelvis is secured to the seat with belts. Subjects are instructed to cross their arms in front of the chest during the experiment, effectively concentrating the mass of the upper body. Thus, the lower body and upper body may each be considered as rigid body segments. The lumbar spine acts as a pivot between the lower and upper body segments where the center of rotation is assumed to be located between the fourth and fifth lumbar vertebra. Given these assumptions, a person sitting on the wobble chair has four degrees of freedom (d.o.f.). Two of these d.o.f. are due to the forward and backward rotation of the lower body and upper body, θ_S and θ_T , respectively. The remaining two d.o.f. are due to the left and right rotation of the lower and upper body, ϕ_S and ϕ_T , respectively. Thus, the state of the system may be described using an eight-dimensional state space (positions and velocities).

4 Wobble chair mathematical model

A mathematical model for the wobble chair can be developed using two rigid body segments [43]. The lower segment would be attached to a freely moving ball joint with stabilizing springs attached to the segment. The upper segment would be attached to the lower segment with an actuated ball joint simulating neuromuscular control of the lumbar spine. Control would be applied between the segments to stabilize the

Fig. 9 The reduced order model of the wobble chair consists of a planar inverted pendulum with stabilizing springs and a limited gain control

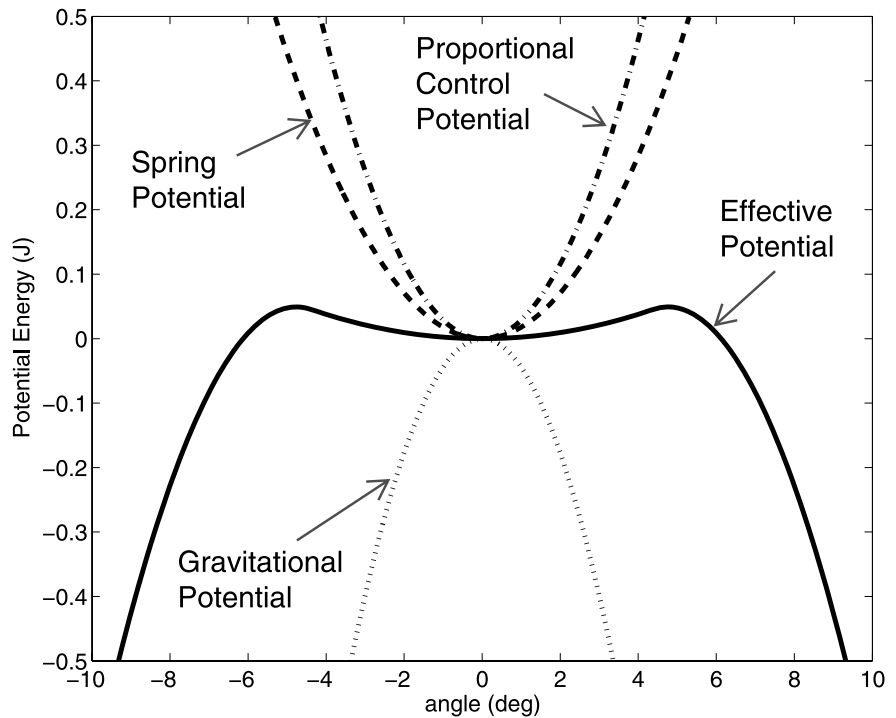


system. Under-actuated systems of this type have been shown to be controllable [44, 45]. However, the system dynamics are quite complex. Therefore, a simpler model will be used, as this will more easily illustrate the new method for separatrix detection, which is the primary purpose of the paper.

A reduced model (Fig. 9) is developed for the wobble chair by restricting movement to the sagittal plane and fixing the angle between the lower body and upper body. These constraints allow the system to be modeled as a planar inverted pendulum, where $\theta_S = \theta_T = \theta$. Stabilizing springs like those used in the actual wobble chair are included in the model. In addition, a limited gain proportional-derivative control is incorporated, which allows the system to have a stable equilibrium point at the upright vertical position. The existence of this stable region was observed in wobble chair experiments where participants were able to balance for 60 seconds in a statically unstable configuration [39]. The effect of the control torque on the motion of the upper body relative to the lower body is approximated in the reduced model as a torque applied at the base. These constraints effectively reduce the wobble chair model from an 8-dimensional to a 2-dimensional state space system. Indeed, even the 8-dimensional state space is only an approximation to a high fidelity continuum mechanics model of the human body.

In addition to reducing the computation time, model reduction allows visualization of system properties that may not be as apparent in higher dimensions. This is the case with LCSs. In the reduced model, LCSs are readily apparent as curves (sometimes broadened curves, or strips) partitioning 2-dimensional state space. However, in the higher order model, it is difficult to visualize LCSs since they are 7-dimensional hyper-surfaces partitioning 8-dimensional state space.

Fig. 10 The effective potential energy function is the sum of the individual components. Under some conditions, a potential well develops near the equilibrium point



The reduced order model, hereafter referred to simply as “the model,” is governed by the following differential equation:

$$\ddot{\theta} = \frac{1}{mh^2}(mgh \sin \theta - kd^2 \sin \theta - C(\theta, \dot{\theta}) + N) \quad (9)$$

where, $\ddot{\theta}$, m , g , h , θ , $\dot{\theta}$, k , and d are the angular acceleration, mass, acceleration of gravity, height, rotation angle, angular velocity, spring stiffness, and the distance of the springs from the central ball joint, respectively. System noise, N , is a zero-mean Gaussian random function which will be discussed in more detail in a later section. The equation for the limited gain proportional-derivative control, C , is given by

$$C(\theta, \dot{\theta}) = G_d \dot{\theta} + \begin{cases} G_p \theta & \text{if } |\theta| < \theta_{cr}, \\ T_{p_max} & \text{otherwise,} \end{cases} \quad (10)$$

where G_d is the derivative gain constant, $\theta_{cr} = T_{p_max}/G_p$ is the smallest angle at which the maximum gain is achieved, G_p is the proportional gain constant, and T_{p_max} is the maximum torque producible by proportional gain. Physiologically, a limited gain controller represents the limited muscle strength of the abdominal and spinal extensor muscles.

Insight into the system’s behavior can be gained by examining the effective potential function

$$\begin{aligned} V_{eff}(\theta) &= mgh \cos \theta - kd^2 \cos \theta \\ &+ \begin{cases} \frac{1}{2} G_p \theta^2 & \text{if } |\theta| < \theta_{cr}, \\ \frac{1}{2} G_p \theta_{cr}^2 + T_{p_max} |\theta - \theta_{cr}| & \text{otherwise,} \end{cases} \end{aligned} \quad (11)$$

which is the sum of the potential functions due to the springs, gravity, and the position-dependent portion of the control (Fig. 10). When the distance between the stabilizing springs and the central ball joint is smaller than a certain threshold value, the upright vertical position is unstable. As the springs are moved further out, the upright vertical position remains unstable until the threshold of stability is reached, i.e., until a certain spring distance is reached. Upon reaching the threshold of stability, a well forms in the effective potential curve in the neighborhood of the upright vertical position. This well leads to a basin of stability in state space. The size of the well may be enlarged by increasing the restorative torque provided by the springs or the controller gain.

Table 1 Parameter table

Parameter	Value	Source
m	69 kg	Typical subject
g	9.81 m/s ²	Typical subject
h	43.0 cm	Calculated from ∇G
k	10,900 N/m	Wobble chair
d	10.35 cm	Value to generate 40% ∇G
G_d	1 Nm/(rad/s)	Calibration parameter
G_p	190 Nm/rad	Calibration parameter
T_{p_max}	14.5 Nm	Calibration parameter

Physiologically, the well allows the participant to balance near the vertical position, remaining stable even under small perturbations due to noise. However, the accumulation of many small perturbations leads to effectively large displacements in state space away from the upright vertical location. When the well's dimensions in state space are exceeded, the participant falls away, seemingly repelled from the vertical position. Thus, the well is of finite size and the vertical position is not globally stable.

The model was calibrated to match anthropometric data of a typical participant performing tests on the wobble chair (Table 1). In order to calibrate the apparatus for a specific participant, the gravitational gradient of the subject is determined. The gravitational gradient, ∇G , is defined as $\frac{\partial M_g}{\partial \theta}$, where M_g is the moment about the pivot due to gravity. ∇G is a function of the participant's body mass and mass distribution. An important indicator of the participant's neuromuscular control capability is the threshold of stability. This parameter is the minimum value of the restorative force (i.e., spring distance) at which the participant is able to maintain balance on the wobble chair for the duration of the test. Its value is expressed as a percentage of ∇G . Pilot data collected from two healthy subjects yielded a typical value of 35% ∇G . The model was calibrated by modifying the controller values, G_p and T_{p_max} , so that the threshold of stability matched the value found experimentally.

In both the mathematical model and wobble chair experiment, angular position data are available for each d.o.f. of the system. Since the velocities can easily be calculated from position data, all dimensions of state space are available. As a result, there is no need to reconstruct state space using the method of delays, as others have done. For the mechanical sys-

tem being modeled, we take the measured coordinates (q) and numerically construct the time derivatives (\dot{q}). These parameters form the n -dimensional state space of $x = (q, \dot{q})$. For the reduced order model, $n = 2$, $q = \theta$, and $x = (\theta, \dot{\theta})$.

Although a mechanically motivated state space reconstruction was performed for the example system in this paper, we note that the method of using an FTLE field to find LCSs is not tied to any particular means of state space reconstruction.

5 Simulations and comparison of LCS detection methods

In this section, nonlinear analysis techniques are applied to detect LCSs under different model conditions and using different detection techniques. First, the parameters of the human postural control model will be set so that the system is deterministic and conservative. Traditional methods will be used to show how the LCSs calculated from vector field data align with a heteroclinic cycle connecting the two hyperbolic points in the model. Second, random noise and a damping component will be introduced to this deterministic model and the LCSs will be detected using traditional methods. The resulting LCSs will be compared to the noise-free LCSs to demonstrate the noise sensitivity of the system. Third, a forward dynamic simulation will be used to generate time series data based on the model. The new methods described in Sect. 2 will be applied to the time series data to obtain LCSs in order to demonstrate that LCSs can be found without a vector field. Sensitivity analyses will be conducted to show the dependency on analysis parameters (e.g., evolution time, δq , and number of trials). Since this paper is focused on the development and evaluation of new methods for LCS detection, the sensitivity and response to changes in controller parameters (G_p and T_{p_max}) associated with neuromuscular control and physiological capability will not be assessed herein and will be reserved for further publications.

5.1 Deterministic and conservative simulation

For the deterministic and conservative simulation, the system noise and damping function of the controller are set to zero. Since the system under these conditions is conservative, the heteroclinic cycle can be determined by generating an iso-energy contour in state

space where the total energy is equal to the maximum effective potential energy. The heteroclinic cycle along with lower and higher energy orbits are shown in Fig. 11. In this example, the heteroclinic cycle forms an eye shaped curve connecting the two saddle points.

Using MATLAB, a vector field is generated from a regular grid (200 by 200) of points in state space centered around the upright vertical position over a range of $\pm 15^\circ$ by $\pm 15^\circ/s$. Each of these points are taken as an initial condition to determine the flow map over a fixed time T from the vector field. The differential equation (9) is solved using a Runge–Kutta (4, 5) ordinary differential equation solver function (MATLAB function ode45). The forward time flow map for the system is seen to correlate well with the iso-energy orbits, as expected.

The FTLE is calculated for each point on the interior of the grid based on the expansion of the state transition matrix. These results are combined over state space to produce a FTLE field. The FTLE field was first calculated by flowing time forward $T = 3$ s. Recalling that LCSs are ridges of the FTLE field, these structures form a “volcano shape” in the 3-dimensional view (Fig. 11(b)). A ridge is formed around the heteroclinic cycle which separates stable motion near the upright vertical position from unstable motion further from the origin in state space. In addition, two other LCSs are noticeable.

In the lower right quadrant, a LCS reveals a hyperbolic surface [19] that is aligned with the iso-energy line associated with the heteroclinic cycle. As the trajectory approaches the heteroclinic cycle, the flow on either side of the LCS splits. Physically, this represents initial conditions beginning in the unstable region with large angles and large negative angular velocities. As the trajectories approach the heteroclinic cycle, those trajectories on the right side of the LCS have insufficient kinetic energy to reach the stable region of state space before achieving zero velocity. As time progresses, these trajectories fall back in the direction from which they came. Trajectories on the left side of the LCS have sufficient energy to approach the upright vertical position. In fact, these trajectories have too much energy to enter the stable region of state space, and they pass over the vertical position to the other side. For the conservative and deterministic system, no approach exists from the unstable region of state space that results in an orbit within the stable region. The LCS forms an impenetrable transport barrier between the two regions. The LCS in the upper

left quadrant describes motion analogous to the LCS in the lower right quadrant, but approaching from the other side.

LCSs can also be generated for the backward flow of time (Fig. 11(c)) where $T = -3$ s. In this case, the LCSs indicate divergence of the backward time flow which can be equally viewed as convergence of the forward time flow. Once again, LCSs are observed to correlate with the curve associated with the heteroclinic cycle. Notice that LCSs are also present around the heteroclinic cycle in the backward time flow. Thus, this separatrix exists in both temporal orientations (i.e. it is not an attractor of trajectories). An LCS associated with convergence is observed in the upper right quadrant. Physically, this LCS represents the convergence of two groups of trajectories. Trajectories to the right of the flow approach the LCS after having insufficient energy to reach the heteroclinic cycle. Flow lines to the right of the LCS originally approached from the opposite side, passed over the upright vertical position, and continued past the stable region with too much energy to stop. These two trajectories converge with each having only slightly different energies. Like the forward time flow, LCSs also form an impenetrable barrier between the two regions in the backward time flow.

Depending on the system, LCSs may have different interpretations. In this case, LCSs form a boundary or separatrix between the region of stable postural sway (around the origin) and unstable falling motion (beyond the boundary). In this biological example, the characteristics of the stable region and its boundary location depend on the accuracy of a number of neurological sensory systems, the feedback gain associated with core muscle strength, and the time delay of the postural control system.

5.2 Deterministic simulation with noise

In the previous section, the noise level and the damping component were set to zero making the system deterministic and conservative. In this section, noise and damping are introduced to better approximate the actual system. System noise, N , is introduced into the model as random force perturbations. It is simulated by a zero-mean Gaussian normal distribution with a standard deviation, σ , equal to 1% of ∇G . Constraints are included in the program to bound the noise level to an amplitude of $\pm 3\sigma$. A noise frequency (20 Hz) is selected such that it substantially exceeds the natural

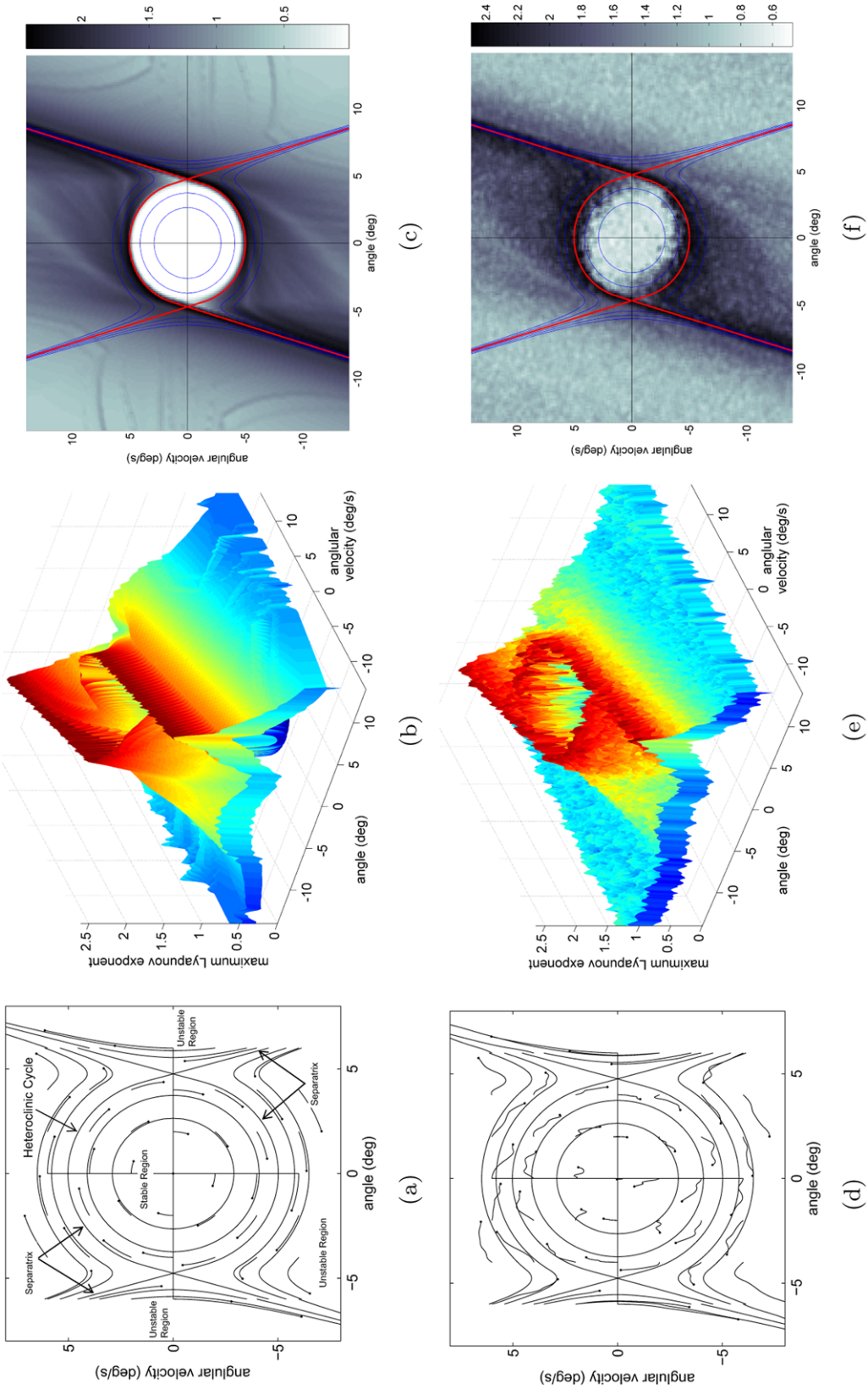


Fig. 11 Analysis results using traditional methods to compute LCS. (a) Iso-energy lines and the flow map ($T = 0.3$ seconds) are shown for the deterministic conservative simulation. The small line segments are the individual trajectories, and the final condition is shown as the dot. LCSs are observable in both the (b) forward time flow (shown in 3D; $T = 3$ seconds) and (c) reverse time flow (shown in 2D; $T = -3$ seconds) FTLE fields. When noise and damping are added to the system, (d) the flow map, (e) forward time flow FTLE field and (f) reverse time flow FTLE field are less smooth, but LCSs remain in the same locations

frequency of the system ($< \sim 3$ Hz). Physiologically, noise can be introduced into the system from muscle twitches, inaccurate motor unit activation, involuntary movements, or external environmental forces [46–48]. Taking these factors into account in (9), the flow map is generated (Fig. 11(d)). For reference, the iso-energy orbits for the conservative deterministic system are overlain.

The damping has the effect of reducing the system energy, attracting trajectories toward the origin. This is observed as a slight inward arching of the flow paths over the 0.3 second evolution time. Random noise slightly perturbs the trajectories as they evolve making the system no longer deterministic. This has the potential to have a dramatic effect on the future of a trajectory. Trajectories near a LCS may be perturbed to the opposite side crossing the barrier. Thus, stable trajectories may become unstable, and unstable trajectories may become stable. Shifts may also occur over the hyperbolic surfaces. The forward and backward time flow plots are shown for the noisy damped configuration. Notice that the perturbations cause the LCSs to be less distinct than the noise-free LCSs. However, the location of the LCSs is unaltered, and it is still very noticeable despite the presence of noise.

5.3 Generation of simulated experimental data

During wobble chair experiments, system noise causes the person to sway, and neuromuscular control effort must be applied to maintain a stable upright posture. The angle is recorded for each segment (lower and upper body) typically at a frequency of 100 or 1000 Hz. When the stabilizing springs are located at a challenging distance, the person attempting to balance on the wobble chair exhibits both stable recoveries and unstable loss of balance resulting in contact with the positive stop at $\pm 15^\circ$.

A forward dynamic simulation is used to generate simulated time series data for analysis and comparison with the results found for the deterministic and conservative simulation. The simulation was generated using MATLAB and is based upon the model. As a result, the time series data shares the same underlying deterministic behavior as the vector field, although this behavior is masked by random noise. Each simulation begins at the origin in state space and is perturbed with Gaussian random force perturbations. These forces generate movement that is attenuated by

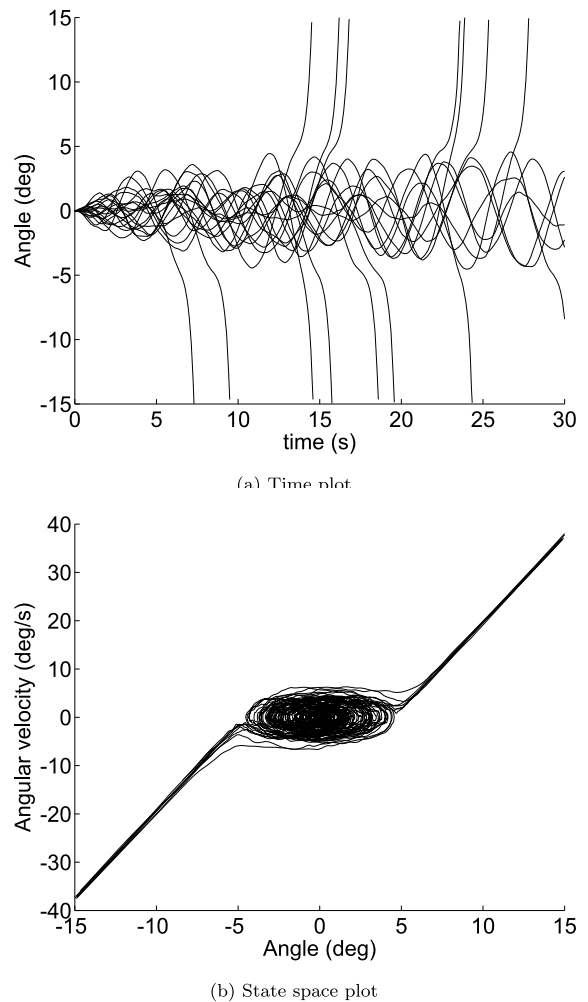


Fig. 12 The time-series data set generated from 20 simulated experimental trials. **(a)** Time plot shows each trials beginning from the state space origin. **(b)** State space plot shows trajectories near the state space origin and projecting to the upper right and lower left

a controller. As a result, the system is able to maintain stability for a period of time before a sequence of perturbations causes the system to become unstable (unrecoverable). Physiologically, this represents a person balancing on the wobble chair initially having a tilt angle and angular velocity equal to zero. Movement begins and the person spends time balancing near the equilibrium point, recovering balance for a time, and eventually falling.

Each simulated trial lasts 30 seconds or until the trajectory becomes unstable and diverges beyond a certain threshold, well into the falling region ($\pm 15^\circ$).

Twenty independent trials are generated and the results are concatenated to form a single data set (Fig. 12).

Prior to analysis, the data set is filtered at 6.37 Hz with a 7th order low pass Butterworth filter and down-sampled to 20 Hz. This is the same technique applied to wobble chair data collected during experiments. It filters out high frequency noise that is not representative of body movement. Moreover, it reduces the size of the data set to improve the speed of computation while maintaining the real trajectory details. With the simulated trajectory now generated and preprocessed, it is possible to conduct the numerical analysis using the two new methods to detect LCSs.

5.4 Nearest neighbor method applied to time series data

The simulated experimental data are analyzed with MATLAB to find the FTLE field using the NN method (Fig. 13(a)–(f)). Unlike the vector field simulations presented earlier that map the flow over the entire state space, the simulated experimental data only contain information about the portion of state space where the trajectories have explored. Since the forward dynamic simulation begins at the state space origin and is randomly perturbed from this location, only trajectories that are initially stable and may become unstable are mapped. As a result, the hyperbolic surfaces associated with the approaching unstable trajectory are not present. Despite being less complete than LCSs generated from vector field data, the displayed portion of the LCSs generated from trajectory data are in the same general location as the heteroclinic cycle and LCSs found from the vector field of the underlying conservative system. Although LCSs are visible in the FTLE field, the separation is not well defined and other structures are also present.

When examining the results, one may notice that FTLE field results are shown for regions of state space that are not explored by trajectories; specifically, the regions above and to the right and below and to the left of the data cluster surrounding the origin. The FTLE field in this region does not represent real results but rather artifacts of the surface generation. These artifacts are a result of the interpolation of data between the points clustered near the origin and the slender lines of data extending to the upper right and lower left (Fig. 13). A filter could be applied to the results to diminish these artifacts by removing regions of the FTLE field that are not well-covered by data points.

The sensitivity to evolution time is also investigated in Fig. 13. At T of 0.6 seconds, no clear LCSs are visible; however, structures are present that tend to be symmetric about the origin. Results are slightly better at 1.2 seconds, and by 1.8 seconds the LCSs are clearly visible. These LCSs align well with the heteroclinic cycle and match those found for the deterministic and conservative system. These LCS are still present at 2.4 seconds, but begin to disappear at longer evolution times.

At an evolution time of 3.0 seconds and greater, the region close to the origin shows high values for the FTLE resulting in a loss of the ridge in the FTLE field that forms the LCS. These large FTLE values near the origin may be an artifact of the method used. Since the concentration of data points is highest near the origin, it is likely that a very near neighbor can be found. As the trajectories are evolved and randomly perturbed, the initially very close points will diverge due to the perturbations even if they are to follow generally the same trajectory. As a result, the ratio of the final distance to the initial distance will be high, leading to a large value for the FTLE. In contrast, data points in the sparse regions of state space may not have very near neighbors. Thus, their initial distance will be larger and as the trajectories evolve in the presence of perturbations, the ratio of the final distance to the initial distance may not be as great. In order to minimize this potential effect, a minimum distance for the nearest neighbor could be set for systems that are not purely deterministic. This change should improve the results found for the NN method. Furthermore, it is speculated that improved results will also be obtained if this change is applied to the traditional methods used to calculate the maximum Lyapunov exponent.

5.5 State transition matrix method applied to time series data

The simulated experimental data are also analyzed using the STM method (Fig. 13(g)–(l)). The same evolution times investigated with the NN method are used so that comparisons between the two methods can be performed easily. The perturbation distance, δq , is set at 0.02 rad (1.15°) and 0.02 rad/s ($1.15^\circ/\text{s}$). At the shortest evolution time, 0.6 seconds, LCSs begin to form near the ejection regions of state space. These ejection regions are located to the upper right and lower left of the heteroclinic cycle. For short evolution times these

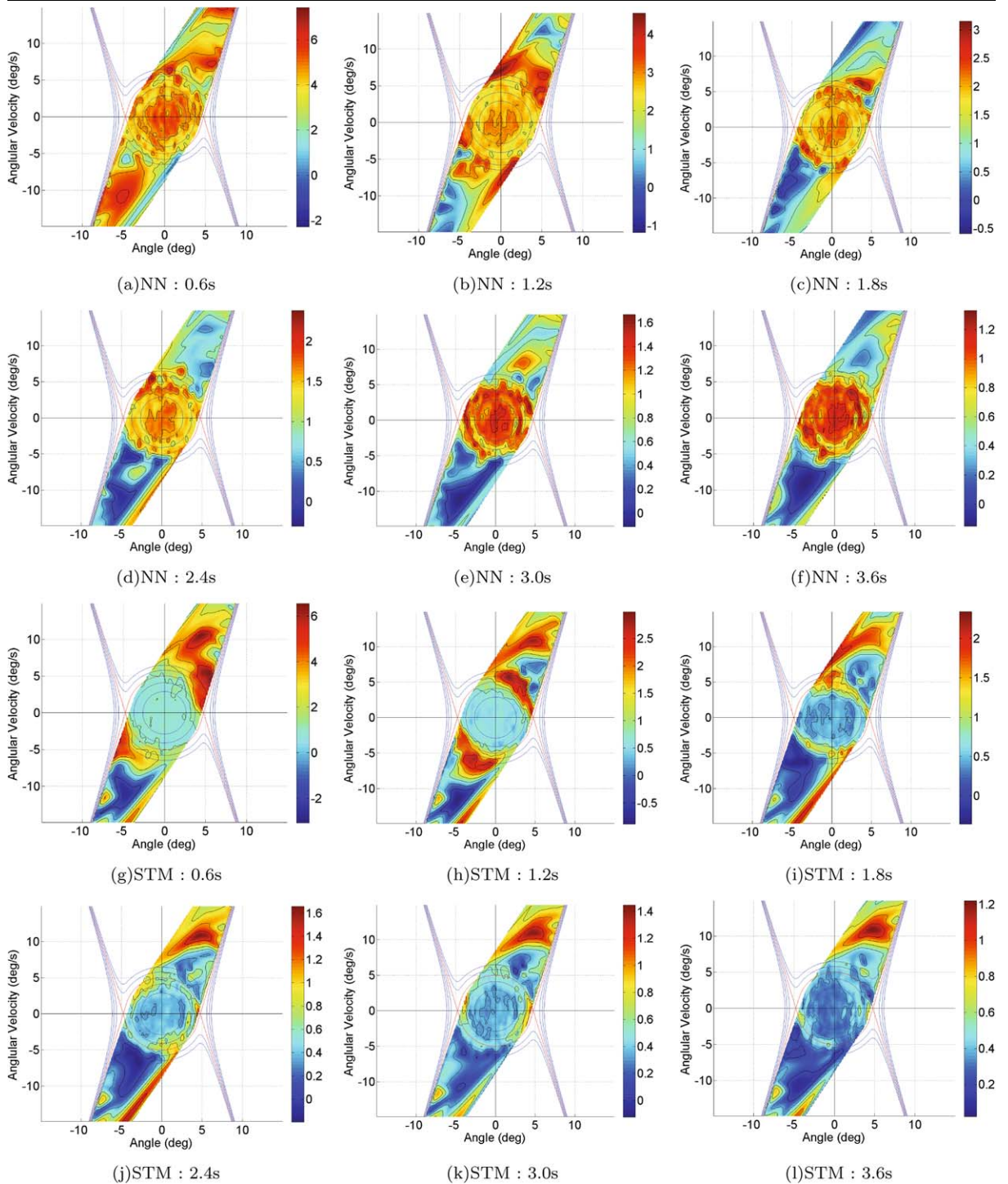


Fig. 13 The Nearest Neighbor method is compared to the State Transition Matrix method at different evolution times (T). FTLE field for evolution times of generated using the NN method showed some noticeable structure. Much better results are obtained using the STM method where the LCS is clearly visible. This structure becomes less apparent at evolution times greater than 2.4 seconds

are the locations where rapid divergence occurs. The resulting LCS is much sharper than that found using the NN method.

For a longer evolution time, 1.2 seconds, the LCSs align well with and now cover the first and third quadrants of the heteroclinic cycle. The dominant peaks of the LCSs shift further to the left on the upper portion of the heteroclinic cycle and further to the right on the lower portion. This apparent counterclockwise rotation is expected since trajectories that are further from the ejection point now have enough time to reach it (refer also to Fig. 3). In order to better explain this concept, consider a cloud of points in the upper left quadrant centered on the heteroclinic cycle with portions of the cloud on each side. As time marches on, each portion of the cloud travels in a generally clockwise direction while the cloud deforms and rotates. However, since the underlying deterministic trajectories are essentially parallel in this region, the cloud generally maintains its shape for a period of time. Upon reaching the ejection point near the tip of the heteroclinic cycle (i.e., the hyperbolic point), the underlying deterministic trajectories diverge leading to rapid expansion of the cloud. As a result, trajectories originating from the upper left quadrant require longer evolution times before the LCS is noticeable. A similar condition exists for identifying the LCS in the lower right quadrant.

For an evolution time of 1.8 seconds the visible portion of the LCSs continues to rotate in the counter clockwise direction leaving less noticeable structure near the ejection points. The reason that the LCSs become less visible near the ejection point at longer evolution times is a result of the way that the time series was generated. In the actual wobble chair experiments, physical stops are present that limited angular displacement to $\pm 15^\circ$ for safety purposes. This limitation is also placed on the simulated time series data. In addition, when people contact the stop during an experiment, they apply a force against the base to propel themselves back toward the state space origin. This property is simulated by concatenating multiple trials to form a single data set. As a result of these effects, when trajectories are evolved for longer times and the angle exceeds 115° , these trajectories jump to the beginning of the next trial. This diminishes the FTLE since these divergent trajectories are effectively merged back with the stable trajectories.

As the evolution time is increased further, the visible region of the LCSs continues to rotate in the counterclockwise direction. By $T = 3.6$ s, the LCSs are

no longer visible. Since the trajectories are allowed to evolve unbounded in the deterministic and conservative simulation, longer evolution times do not diminish the results near the ejection point. This is the reason that full LCSs are visible at the relatively long evolution time of 3.0 seconds in Fig. 11. Since the STM method yields better results than the NN method, further investigation into the sensitivity is performed on the STM method only. In order to easily compare the sensitivity of different parameters, a “standard” for comparison is established as follows: (1) Analysis using the STM method, (2) $\delta q = 0.02$ rad (1.15°) and $\delta \dot{q} = 0.02$ rad/s, and (3) a 20-trial simulation data set. This “standard” is included in every set of figures in which parameter sensitivity is evaluated.

5.6 Sensitivity to cloud size, δq

The choice of δq , the radius of the cloud of initial locations in state space, influences the FTLE field (Fig. 14). However, parameter sensitivity analysis shows this method to be relatively insensitive to the value of δq . The perturbation distance δq is a coarse-graining parameter selected to be large enough to overcome system noise and small enough to reveal local features of the FTLE field. Typically, δq would need to be normalized to account for difference in scale between the angle and angular velocity. However, in this analysis the range of the angular velocity approximates that of the angle, so normalizing the angular velocity is unnecessary.

Sharp and well defined LCSs are obtained using the “standard” for comparison, $\delta q = 0.02$ rad (1.15°) and $\delta \dot{q} = 0.02$ rad/s. A reduction in the value of δq by a factor of 20 reduced the smoothness of the FTLE field and introduced new artifacts, but did not change the locations of the LCSs. Increasing the value of δq to 0.05 also reduces the quality of the results by decreasing the distinctness of the LCS. The reason for the apparent loss of sensitivity at a $\delta q \geq 0.05$ may be an inability to detect local structure since the cloud diameter increased to over 5° , over half the diameter of the stability basin (in the θ direction).

5.7 Sensitivity to data quantity

Although 20 trials were evaluated as the “standard,” a separate simulation indicates that portions of the basin boundary may be identified (albeit with low precision)

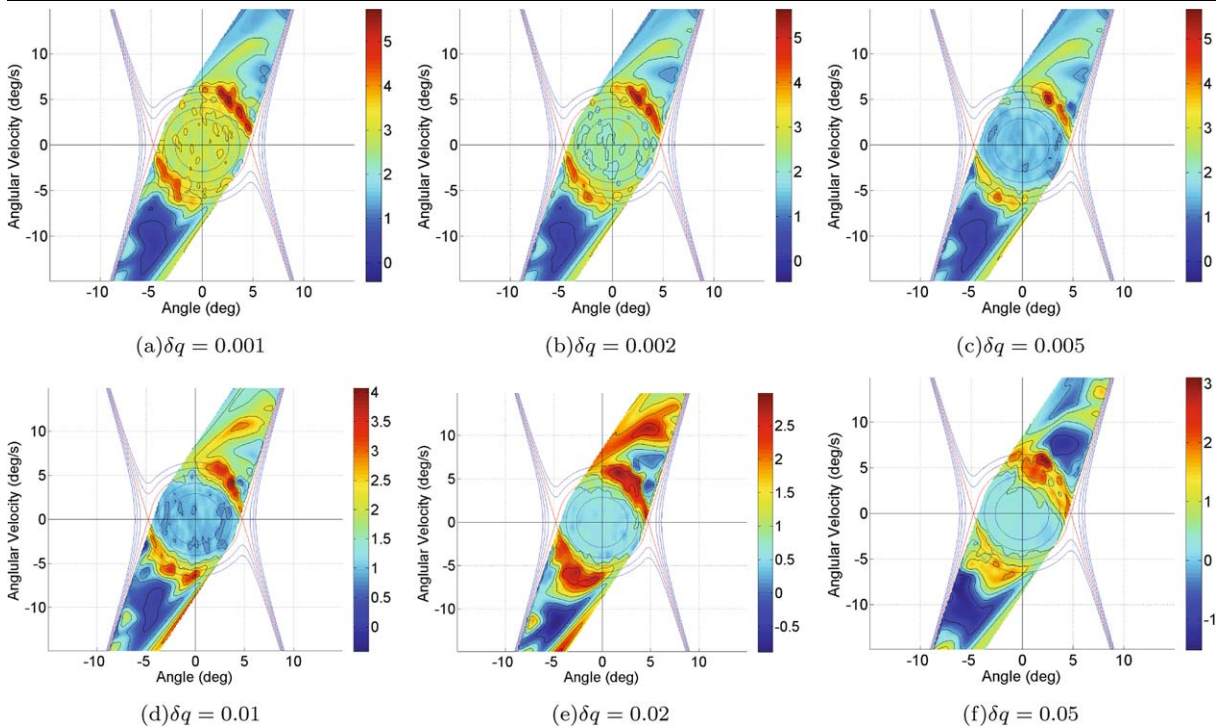


Fig. 14 Sensitivity of the analysis to cloud size (parameterized by the δq). The “standard” size of δq is 0.02 rad (1.15°) and 0.02 rad/s (1.15°/s) (given in (e)). This parametric analysis showed minimal differences over the range of δq explored

with as little as two trials using this method (Fig. 15). Yet, not every data set with only two trials will reveal an LCS. For an LCS to be noticeable, both trials must become unstable, thus exploring regions of state space beyond the stable region. In addition, since comparisons are made between neighbors, both trials must diverge in the same direction. In Fig. 15(a), a data set consisting of two trials that both diverged to the lower left quadrant is evaluated. Structure is noticeable at the location of the heteroclinic cycle but LCSs are not sharply defined. With only two trials, the results tend to be more affected by random noise. Furthermore, it is more difficult to find neighbors in each orthogonal direction for the development of an appropriately shaped cloud of points due to low data point density.

Increasing the number of trials in the data set to five, the FTLE field is able to extend in both directions. Like the data set evaluated previously, the 5-trial data set was selected such that at least two trials diverged in each direction. As a result, the sharpness of the LCS is not much better than the 2-trajectory data set evaluated previously. A 10-trial data set yields a more complete view of the LCS. With 10 trials, there is sufficient

probability to obtain trials that diverge in each direction, so no restrictions were placed on the selection of a trial for analysis. However, upon analysis, results were poorer than expected for 10 trials (Fig. 15(c)). Since the trajectories were generated using a forward dynamic simulation driven by random perturbations, results can be unpredictable. Different simulation data sets would likely yield different sharpness of the LCS, but since the underlying dynamics are the same, the location of the LCS should not change.

The resulting LCSs for the “standard” 20-trial data set are sharp and in the correct location. Expanding the number of trials in the data set to 50 yields results similar to those found for the 20-trial data set. However, the processing time was significantly increased. Processing time was increased because the number of reference points increased by 2.5 times. In addition, the number of data points to evaluate when searching for neighbors also increases by 2.5 times. Overall, these factors lead to a dramatic increase in processing time with no noticeable improvement in results. Increasing the number of trials to 100 actually decreased the distinctness of the LCS. The reason for this effect

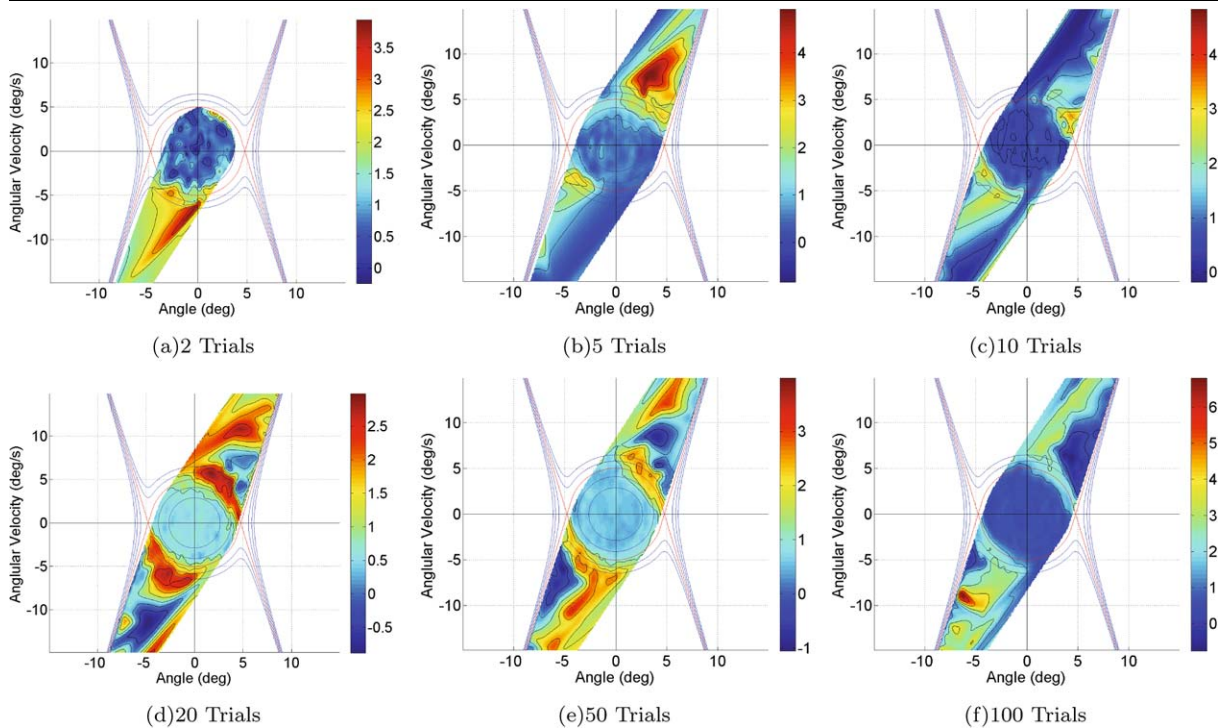


Fig. 15 Sensitivity of the analysis results to the number of trials. With only two trials diverging in the same direction, structure is visible on the side of the divergence. With 5 trials (at least two on each side), structure is visible on both sides. The best results were obtained with at least 20 trials

may be a result of increasing the data point density in the sparse regions of state space which amplify the artifacts associated with transition between one trial and the next. The noticeable large FTLE in Fig. 15(f) at grid coordinate $(-6, -9)$ may be detecting the transition between reaching -15° and jumping back to the origin. It is unknown why another large FTLE is not noticeable at the symmetric location in the upper right quadrant. However, it may be attributed to the random nature of the data sets. We note, however, that LCSs are defined as ridges in the FTLE field, not necessarily field peaks. Using this criterion, there is still a ridge present at the expected location. This suggests that a further refinement of the method to investigate ridge-extraction methods should be performed in future work.

6 Conclusions

In this paper, we have shown how boundaries that separate qualitatively different kinds of motion can be

found using the method of Lagrangian coherent structures applied to time series data. This is distinct from previous approaches to computing LCSs that relied upon a known vector field. Using traditional methods to compute the LCS we demonstrated that the location of LCSs aligned well with the heteroclinic cycle, a separatrix, of the underlying conservative system, even in the presence of system noise. We introduced two new computational methods to find LCSs from time series data; the form of data commonly collected during biomechanics experiments. We calculated FTLE fields from simulated data using both of these methods and demonstrated that the resulting LCSs aligned well with the heteroclinic cycle. In addition, we demonstrated how different regions of the LCS could be found by evaluating different trajectory evolution times. The STM method was determined to be superior to the NN method for the model studied. The STM method was generally insensitive to the size of the cloud of initial conditions and LCSs could be obtained with a small number of trials (~ 20).

Using the LCS approach, we achieved our primary goal of finding boundary structure in the state space

from simulated experimental data; important structure which has gone previously unnoticed. Development of methods to find the precise location of the LCS is left for future work.

In the biological example explored, the LCSs form the boundary of a basin of stability, separating a stable mode from a failure mode. Defining the basin of stability in state space provides a much richer understanding of the system dynamics over previous methods that calculate a single scalar measure of stability, e.g., the state-space-averaged maximum finite-time Lyapunov exponent.

A possible application of boundary detection from experiments is the following. The boundary of the basin of stability, i.e., the recovery envelope, could be used in conjunction with sway data to define new measures of individual fall risk, e.g., the average distance of an individual's state from the boundary.

In forthcoming work, we will demonstrate the method on higher dimensional data and actual experimental data. In general, we believe the method demonstrated in this study provides a fruitful approach for extracting additional information from noisy experimental data, namely boundaries between qualitatively different kinds of motion.

Acknowledgements The authors would like to express their gratitude to the anonymous referees and to Dr. Kevin P. Granata for his contributions and guidance during the early portions of this research. Tragically, Dr. Granata was killed in the Virginia Tech shootings of April 16th, 2007. Although he left this world far too early, his visionary spirit has guided the authors throughout this research.

References

- Dingwell, J.B., Cusumano, J.P.: Nonlinear time series analysis of normal and pathological human walking. *Chaos* **10**(4), 848–863 (2000)
- Akay, M.: *Wiley Encyclopedia of Biomedical Engineering*. Wiley–Interscience, Hoboken (2006)
- England, S.A., Granata, K.P.: The influence of gait speed on local dynamic stability of walking. *Gait Posture* **25**(2), 172–178 (2007)
- Pierrehumbert, R.T.: Chaotic mixing of tracer and vorticity by modulated travelling Rossby waves. *Geophys. Astrophys. Fluid Dyn.* **58**, 285–319 (1991)
- Pierrehumbert, R.T.: Large-scale horizontal mixing in planetary-atmospheres. *Phys. A-Fluids Fluid Dyn.* **3**(5), 1250–1260 (1991)
- Shadden, S.C., Lekien, F., Marsden, J.E.: Definition and properties of Lagrangian coherent structures from finite-time Lyapunov exponents in two-dimensional aperiodic flows. *Phys. D Nonlinear Phenom.* **212**(3–4), 271–304 (2005)
- Haynes, P.: Stratospheric dynamics. *Annu. Rev. Fluid Mech.* **37**, 263–293 (2005)
- Falconer, I., Gottwald, G.A., Melbourne, I., Wormnes, K.: Application of the 0-1 test for chaos to experimental data. *SIAM J. Appl. Dyn. Syst.* **6**(2), 395–402 (2007)
- Benettin, G., Galgani, L., Giorgilli, A., Strelcyn, J.: Lyapunov characteristic exponents for smooth dynamical systems and for Hamiltonian systems; a method for computing all of them. Part I: Theory. *Meccanica* **15**, 9–20 (1980)
- Benettin, G., Galgani, L., Giorgilli, A., Strelcyn, J.: Lyapunov exponents for smooth dynamical systems and Hamiltonian systems; a method for computing all of them. Part II: Numerical application. *Meccanica* **15**, 21–30 (1980)
- Wolf, A., Swift, J.B., Swinney, H.L., Vastano, J.A.: Determining Lyapunov exponents from a time series. *Phys. D Nonlinear Phenom.* **16**(3), 285–317 (1985)
- Eckmann, J.P., Kamphorst, S.O., Ruelle, D., Ciliberto, S.: Lyapunov exponents from time-series. *Phys. Rev. A* **34**(6), 4971–4979 (1986)
- Rosenstein, M.T., Collins, J.J., Deluca, C.J.: A practical method for calculating largest Lyapunov exponents from small data sets. *Physica D* **65**(1–2), 117–134 (1993)
- Kantz, H., Schreiber, T.: *Nonlinear Time Series Analysis*. Cambridge University Press, Cambridge (2004)
- Haller, G., Yuan, G.: Lagrangian coherent structures and mixing in two-dimensional turbulence. *Phys. D Nonlinear Phenom.* **147**(3–4), 352–370 (2000)
- Haller, G.: Finding finite-time invariant manifolds in two-dimensional velocity fields. *Chaos* **10**(1), 99–108 (2000)
- Haller, G.: Distinguished material surfaces and coherent structures in three-dimensional fluid flows. *Physica D* **149**(4), 248–277 (2001)
- Haller, G.: Lagrangian structures and the rate of strain in a partition of two-dimensional turbulence. *Phys. Fluids* **13**(11), 3365–3385 (2001)
- Haller, G.: Lagrangian coherent structures from approximate velocity data. *Phys. Fluids* **14**(6), 1851–1861 (2002)
- Casdagli, M., Eubank, S., Farmer, J.D., Gibson, J.: State-space reconstruction in the presence of noise. *Physica D* **51**(1–3), 52–98 (1991)
- Ellner, S., Turchin, P.: Chaos in a noisy world—new methods and evidence from time-series analysis. *Am. Nat.* **145**(3), 343–375 (1995)
- Franca, L.F.P., Savi, M.A.: Distinguishing periodic and chaotic time series obtained from an experimental nonlinear pendulum. *Nonlinear Dyn.* **26**(3), 253–271 (2001)
- Wang, Y., Haller, G., Banaszuk, A., Tadmor, G.: Closed-loop Lagrangian separation control in a bluff body shear flow model. *Phys. Fluids* **15**(8), 2251–2266 (2003)
- Aldridge, B., Haller, G., Sorger, P., Lauffenburger, D.: Direct Lyapunov exponent analysis enables parametric study of transient signalling governing cell behaviour. *IEE Proc. Syst. Biol.* **153**, 425–432 (2006)
- El Rifai, K., Haller, G., Bajaj, A.K.: Global dynamics of an autoparametric spring-mass-pendulum system. *Nonlinear Dyn.* **49**(1–2), 105–116 (2007)
- Winter, D.A., Patla, A.E., Rietdyk, S., Ishac, M.G.: Ankle muscle stiffness in the control of balance during quiet standing. *J. Neurophysiol.* **85**(6), 2630–2633 (2001)

27. Morasso, P.G., Sanguineti, V.: Ankle muscle stiffness alone cannot stabilize balance during quiet standing. *J. Neurophysiol.* **88**(4), 2157–2162 (2002)
28. Kuo, A.D., Zajac, F.E.: A biomechanical analysis of muscle strength as a limiting factor in standing posture. *J. Biomech.* **26**(Suppl. 1), 137–150 (1993)
29. Pai, Y.C., Patton, J.: Center of mass velocity–position predictions for balance control. *J. Biomech.* **30**(4), 347–354 (1997)
30. Iqbal, K., Pai, Y.C.: Predicted region of stability for balance recovery: motion at the knee joint can improve termination of forward movement. *J. Biomech.* **33**(12), 1619–1627 (2000)
31. Edwards, W.T.: Comments on “Predicted region of stability for balance recovery: motion at the knee joint can improve termination of forward movement”. *J. Biomech.* **34**(6), 831–833 (2001)
32. Granata, K.P., Orishimo, K.F.: Response of trunk muscle co-activation to changes in spinal stability. *J. Biomech.* **34**(9), 1117–1123 (2001)
33. Cholewicki, J., McGill, S.M.: Mechanical stability of the in vivo lumbar spine: implications for injury and chronic low back pain. *Clin. Biomech. (Bristol, Avon)* **11**(1), 1–15 (1996)
34. Truesdell, C., Noll, W.: *The Non-Linear Field Theories of Mechanics*. Springer, Berlin (2004)
35. Fung, Y.: *Biomechanics: Mechanical Properties of Living Tissues*. Springer, New York (1993)
36. Strang, G.: *Linear Algebra and its Applications*. Harcourt Brace Jovanovich, San Diego (1998)
37. Lekien, F., Shadden, S.C., Marsden, J.E.: Lagrangian coherent structures in n -dimensional systems. *J. Math. Phys.* **48**(6) (2007)
38. Tanaka, M.L., Granata, K.P.: Methods & nonlinear analysis for measuring torso stability. In *ASCE 18th Engineering Mechanics Division Conference Blacksburg, VA*, 3–6 June 2007
39. Lee, H., Granata, K.P.: Process stationarity and reliability of trunk postural stability. *Clin. Biomech. (Bristol, Avon)* **23**(6), 735–742 (2008)
40. Lee, H., Granata, K.P., Madigan, M.L.: Effects of trunk exertion force and direction on postural control of the trunk during unstable sitting. *Clin. Biomech. (Bristol, Avon)* **23**(5), 505–509 (2008)
41. Slota, G.P., Granata, K.P., Madigan, M.L.: Effects of seated whole-body vibration on postural control of the trunk during unstable seated balance. *Clin. Biomech. (Bristol, Avon)* **23**(4), 381–386 (2008)
42. Cholewicki, J., Polzhofer, G.K., Radebold, A.: Postural control of trunk during unstable sitting. *J. Biomech.* **33**(12), 1733–1737 (2000)
43. Tanaka, M.L.: *Biodynamic analysis of human torso stability using finite time Lyapunov exponents*. Ph.D. thesis, Virginia Polytechnic Institute and State University (2008)
44. Murray, R., Hauser, J.A.: *Case: Study on Approximate Linearization: The Acrobot Example*. Electronics Research Laboratory, College of Engineering, University of California, Berkeley, pp. 1–43 (1991)
45. Spong, M.W.: The swing up control problem for the acrobot. *IEEE Control Syst. Mag.* **15**(1), 49–55 (1995)
46. Collins, J.J., De Luca, C.J.: Open-loop and closed-loop control of posture: a random-walk analysis of center-of-pressure trajectories. *Exp. Brain Res.* **95**(2), 308–318 (1993)
47. Delignieres, D., Deschamps, T., Legros, A., Caillou, N.: A methodological note on nonlinear time series analysis: is the open- and closed-loop model of Collins and De Luca (1993) a statistical artifact? *J. Mot. Behav.* **35**(1), 86–97 (2003)
48. Bottaro, A., Casadio, M., Morasso, P.G., Sanguineti, V.: Body sway during quiet standing: is it the residual chattering of an intermittent stabilization process? *Hum. Mov. Sci.* **24**(4), 588–615 (2005)